Version of Record: https://www.sciencedirect.com/science/article/pii/S0022283624000159
Manuscript_b95a39d338fcf6f94849ba86f1c9ecbe

Mechanisms of allosteric inhibition of Insulin-Regulated Aminopeptidase

Anastasia Mpakali[1,2], Ioanna Barla[3], Liying Lu[4], Karthik M. Ramesh[4], Nikolaos Thomaidis[3], Lawrence J. Stern[4], Petros Giastas[5], and Efstratios Stratikos[1,2,*]

[1] Laboratory of Biochemistry, Department of Chemistry, National and Kapodistrian University of Athens, Athens 15771, Greece
[2] National Centre for Scientific Research Demokritos, Athens 15341, Greece
[3] Laboratory of Analytical Chemistry, Department of Chemistry, National and Kapodistrian University of Athens, Athens 15771, Greece
[4] Department of Pathology, UMass Chan Medical School, Worcester, MA 01650, USA
[5] Department of Biotechnology, School of Applied Biology & Biotechnology, Agricultural University of Athens, Athens 11855, Greece
*Corresponding author: Efstratios Stratikos, estratikos@chem.uoa.gr or stratos@rrp.demokritos.gr

© 2024 published by Elsevier. This manuscript is made available under the Elsevier user license
https://www.elsevier.com/open-access/userlicense/1.0/

ABSTRACT

Inhibition of Insulin-Regulated Aminopeptidase is being actively explored for the treatment of several human diseases and several classes of inhibitors have been developed although no clinical applications have been reported yet. Here, we combine enzymological analysis with x-ray crystallography to investigate the mechanism employed by two of the most studied inhibitors of IRAP, an aryl sulfonamide and a 2-amino-4H-benzopyran named HFI-419. Although both compounds have been hypothesized to target the enzyme's active site by competitive mechanisms, we discovered that they instead target previously unidentified proximal allosteric sites and utilize non-competitive inhibition mechanisms. X-ray crystallographic analysis demonstrated that the aryl sulfonamide stabilizes the closed, more active, conformation of the enzyme whereas HFI-419 locks the enzyme in a semi-open, and likely less active, conformation. HFI-419 potency is substrate-dependent and fails to effectively block the degradation of the physiological substrate cyclic peptide oxytocin. Our findings demonstrate alternative mechanisms for inhibiting IRAP through allosteric sites and conformational restricting and suggest that the pharmacology of HFI-419 may be more complicated than initially considered. Such conformation-specific interactions between IRAP and small molecules can be exploited for the design of more effective second-generation allosteric inhibitors.

Keywords: Insulin-Regulated Aminopeptidase, inhibitors, enzyme, allosteric, crystal structures, kinetics, mechanism, small-angle X-ray scattering, oxytocin, conformational change.

INTRODUCTION

Insulin-Regulated Aminopeptidase (IRAP, EC 3.4.11.3) is a transmembrane zinc metalloprotease that belongs to the M1 family of metalloproteases and in particular in the oxytocinase subfamily[1]. IRAP has been reported to have several important biological functions that include roles in glucose metabolism through the regulation of trafficking of glucose transporter 4 [2], the degradation of placental oxytocin levels [3], the regulation of immune responses through the generation of antigenic peptides or effects on T-cell receptor signalling [4,5], as well as roles in cognition through the regulation of brain oxytocin and vasopressin [6,7]. IRAP is a transmembrane protein consisting of a small cytoplasmic domain that plays roles in intracellular trafficking and a large extra-cellular domain that carries the aminopeptidase activity. Several potential physiological substrates have been identified to mediate IRAP biological functions. For example, IRAP's role in adaptive immunity is driven by the trimming of precursor antigenic peptides in specialized compartments of antigen-presenting cells performing cross-presentation [8]. Other biological functions of IRAP are likely mediated by the degradation of peptidic hormones. Notably, IRAP can degrade macrocyclic peptides such as oxytocin and vasopressin in the placenta or the brain [3,9]. The latter likely mediates the role of IRAP in cognitive functions [10]. Other possible substrates include angiotensin III, metenkephalin, dynorphin A, neurokinin A, neuromedin B, and somatostatin [11]. Regulation of IRAP's enzymatic activity for pharmaceutical applications using small molecular weight inhibitors has attracted significant experimental efforts, in particular in the area of cognition and treatment of ischemic stroke [10,12–16]. In addition, circulating, soluble IRAP is being actively explored as a biomarker for diabetes, cardio-metabolic diseases and ischemic stroke [17,18].

Over the last decade, several inhibitors of IRAP have been developed and tested in a variety of cellular and *in vivo* systems. These include pseudophosphinic peptide transition-state-analogues, aryl sulfonamides, benzopyran derivatives, diaminobenzoic acid derivatives and cyclic peptide analogues [10,13,19–25]. IRAP inhibitors have been discovered either after rational substrate-inspired design or after random chemical or virtual library screening. In both cases, the proposed mechanism of action is direct competition with the substrate for the catalytic site of the enzyme. Two main classes of IRAP inhibitors discovered by library screening are aryl sulfonamides and benzopyran derivatives[24][25]. Compounds from both

chemical scaffolds have been shown to be active in cellular systems relating to IRAP biological activities. In particular, aryl sulfonamide inhibitors as well as the benzopyran derivative HFI-419 have been shown to enhance spatial working memory by promoting the formation of functional dendritic spines in primary hippocampal neuron cultures, and this effect was proposed to rely on enhanced glucose uptake [14][26]. Most notable, HFI-419 has been utilized in numerous *in vivo* studies and its activity has been associated with biological functions of IRAP such as acetylcholine-mediated vasoconstriction [27], glucose tolerance in insulin-resistant Zucker fatty rats [28], glucose handling in normal and diabetic rats [29] *in vivo* Leucine Enkephalin Hydrolysis [30] and ischemic stroke[16]. Despite these results, however, no clinical application of an IRAP inhibitor has been reported yet.

Of the IRAP inhibitors reported, aryl sulfonamides and benzopyran derivatives, such as compound HFI-419, are of particular interest pharmacologically because they carry a good selectivity profile, and they are not of peptidic nature and thus can avoid common pharmacokinetic pitfalls of peptidic inhibitors. The mechanism of action of these compounds has been investigated by biochemical and computational studies and the most commonly proposed mode of action is a competitive mechanism through the occupation of the catalytic site and chelation of the active-site zinc(II) atom by the sulfonamide group and either an oxygen atom in position 3 or the nitrogen atom of the pyridine ring of the benzopyran derivative [24,29,31–33] In one study, alternative non-competitive mechanisms of inhibition were suggested for specific analogues but experiments were carried out using membrane preparations of the enzyme complicating interpretation [14]. For benzopyran derivatives, site-directed mutagenesis suggested that Phenylalanine-544, a residue lining the S1 specificity pocket of the enzyme, is important for inhibitor binding by forming p-stacking interactions with the main aromatic rings of the compound [33]. These mechanistic insights are guiding the further development of these two chemical scaffolds.

The extra-cellular aminopeptidase component of IRAP has been studied by X-ray crystallography revealing four structural domains that organize into a concave structure that hosts the catalytic site adjacent to an internal large cavity [34][35]. One of those structures contained a peptidic substrate analogue that extended from the catalytic site, throughout the length of the cavity towards the external solvent [34]. Structures solved more recently, in complex with a phosphinic pseudopeptide inhibitor, a macrocyclic peptidic inhibitor and a bestatin analogue, revealed that IRAP can change conformation and assume a more closed

configuration in which the active site and the adjacent large cavity are isolated in the interior of the protein with no direct access to the external solvent [36–38]. Significant structural reconfigurations in the active site, including the reorientation of a catalytic Tyrosine residue and the GAMEN motif, were linked to this conformational change and proposed to differentiate the two conformations in terms of enzymatic activity, with the closed conformation considered to be more active due to optimized configuration of its catalytic site elements. Analysis by small-angle X-ray scattering suggested that IRAP is primarily in the open conformation in solution and undergoes conformational closing upon inhibitor binding [37]. The role and importance of this conformational flexibility to the mechanism of inhibition by non-peptidic classes of inhibitors have not been investigated.

In this study, we explored the mechanism of action of an aryl-sulfonamide inhibitor of IRAP as well as the benzopyran derivative HFI-419, which is widely used in *in vivo* experiments as a tool compound. By a combination of enzymatic kinetic analyses and x-ray crystallography, we show that, in contrast to what has been proposed before, both compounds do not operate by binding in the active site and engaging the catalytic zinc(II) atom, but rather bind to nearby allosteric sites. In particular, HFI-419 appears to lock the enzyme to the open and less active conformation by bridging domains I and IV and sterically blocking further closing. Surprisingly, although HFI-419 is a potent inhibitor of a small dipeptidic substrate commonly used in previous studies, it was found to be unable to block the degradation of the physiological IRAP peptide substrate, oxytocin, an observation consistent with its binding site and preferred conformation. Our data, taken together, allow us to propose a structural and kinetic framework for IRAP function and inhibition and suggest that *in vivo* and *in cellulo* results obtained using HFI-419 may need to be re-evaluated in the context of targeted physiological IRAP substrates.

RESULTS

In vitro potency of compounds

To investigate the mechanism of inhibition of the two compounds we first characterized the inhibitory potency using a recombinant version of the extracellular component of IRAP, which carries the aminopeptidase activity (Figure 1)[39]. Both compounds, N-(3-(1H-tetrazol-5-yl)phenyl)-4-bromo-5-chlorothiophene-2-sulfonamide (compound **1**) and ethyl 2-acetamido-7-hydroxy-4-(pyridin-3-yl)-4H-chromene-3-carboxylate (compound **2**) were found to be potent inhibitors of the hydrolysis of the dipeptidic substrate L-Leucine-7-amido-4-methylcoumarin at the nM level. Compound **1** was found to have an IC_{50} value of 207 nM and compound **2** had an IC_{50} value of 397 nM. While the measurement for compound **2** is in line with previous determinations [40], we found compound **1** to be about 10-fold more potent than previously determined [25]. This could be because previous determinations of inhibitory potency were performed using either the hamster version of IRAP from Chinese Hamster Ovary cells or the full-length enzyme in crude membranes isolated from transiently transfected HEK293 cells, versus the purified human aminopeptidase domain of IRAP used for our measurements [25,32].

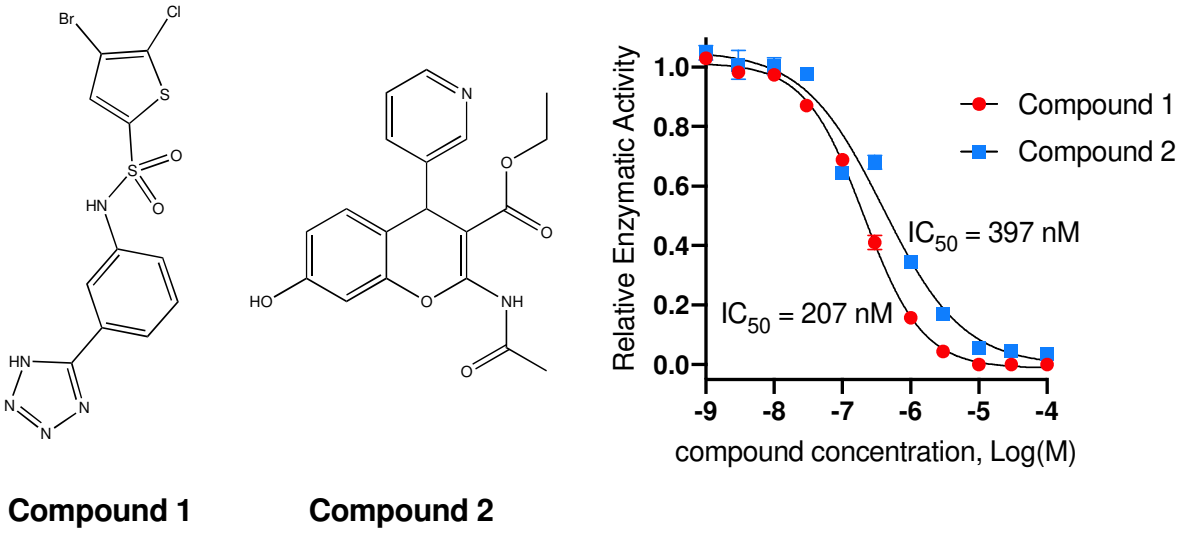

Figure 1: Left, chemical structures of the two IRAP inhibitors analyzed, N-(3-(1H-tetrazol-5-yl)phenyl)-4-bromo-5-chlorothiophene-2-sulfonamide (compound **1**) and ethyl 2-acetamido-7-hydroxy-4-(pyridin-3-yl)-4H-chromene-3-carboxylate (compound **2**). Right, titration of each compound blocks hydrolysis of L-Leucine-7-amido-4-methyl coumarin by IRAP in a dose-dependent manner and an IC_{50} = 207 nM and 397 nM respectively.

Michaelis-Menten analysis – Mechanism of inhibition

To explore the mechanism of action of the two compounds we performed Michaelis-Menten analysis (Figure 2). Although most studies have suggested these compounds to be competitive inhibitors, we observed that both compounds reduced the k_{cat} of the enzyme in a dose-dependent manner, which is inconsistent with competitive mechanisms. Furthermore, the compounds had a distinct effect on the K_M constant, with compound **1** demonstrating a non-significant effect whereas compound **2** significantly reduced the K_M value (Figure 2A-B and Figure 2C-D). Lineweaver–Burk plots confirmed this behaviour (Figures 2C and 2F). Increasing substrate concentration had a non-significant effect on inhibitor potency for compound **1** but did slightly enhance inhibitor potency for compound **2** suggesting allosteric effects (Supplemental Figure S2). Based on this analysis, compound **1** would be characterized to be a non-competitive inhibitor suggesting that it binds at an allosteric site and can interact with both the free enzyme and the enzyme-substrate complex but leads to a non-productive inhibitor-enzyme-substrate complex. Conversely, compound **2** would be characterized as an uncompetitive inhibitor, suggesting that it also binds at an allosteric site reducing catalytic efficiency but also indirectly affecting the binding of the substrate. Both mechanisms suggest that the compounds bind in allosteric sites, in sharp contrast with previous reports based on computational methods that had suggested that both compounds bind at the active site of IRAP and engage the catalytic zinc(II) [31,32].

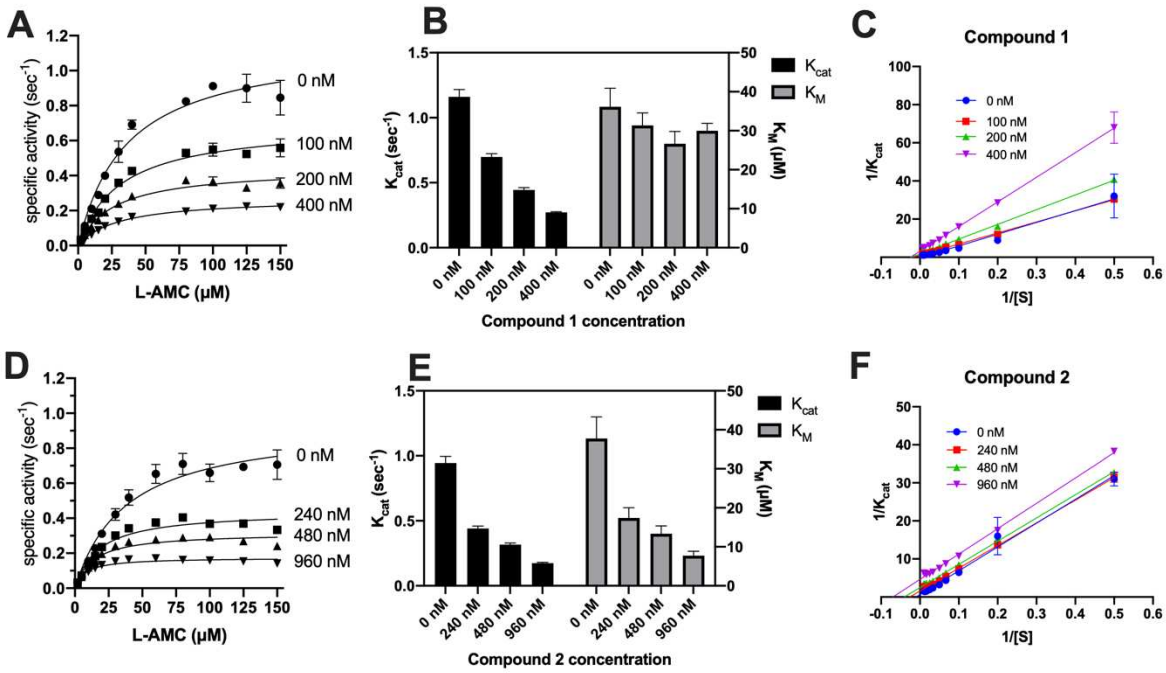

Figure 2: Michaelis-Menten analysis of IRAP in the absence or presence of compounds **1** (Panels A-C) and **2** (Panels D-F) performed at 50 μM L-AMC substrate concentration. ***Panels A** and **D***, specific activity of IRAP as a function of substrate concentration in the presence of increasing amounts of compound (compound **1**, panel A; compound **2**, panel B). Data were fit to a simple Michaelis-Menten model. ***Panels B** and **E***, calculated parameters k_{cat} and K_M for different concentrations of the inhibitors (compound **1**, panel B; compound **2**, panel E). **Panels C and F,** Lineweaver–Burk plots of data presented in Panels A and D.

Crystal structures reveal allosteric binding sites

To understand the surprising kinetics of inhibition for compounds **1** and **2**, we co-crystalized the compounds with the soluble extracellular aminopeptidase domain of IRAP and solved the crystal structures at 2.6 Å and 3.03 Å respectively (Figure 3 and Supporting Table 1). In both cases, we did not detect sufficient additional electron density at the active site adjacent to the catalytic zinc(II) atom that could be attributed to the ligand, suggesting that neither inhibitor occupied the active site, consistent with the conclusions of the enzymatic analysis. Rather, sufficient additional density for compound **1** was detected near to, but not occupying the active site, 7 Å away from the zinc(II), and sufficient additional density for compound **2** was located 14 Å away (Figure 3A-C and Supporting Figure S1). Specifically, the tetrazole moiety of compound **1** was found to make pi-stacking interactions with Phe550 and Tyr495 and potential H-bonding interactions with Lys460 and Glu494 which lined a shallow pocket P1 (Figure 3B and 3D). The 3-bromo-2-chlorothiophene moiety of compound **1** was found to be accommodated in a shallow hydrophobic pocket and make

pi-stacking interactions with Phe544 (Figure 3C and 3E). Compound **2** was found in between domain II and domain IV of the enzyme, primarily making van der Waals shape complementarity contacts with domain II, and pi-stacking contacts with Phe544 and Tyr272 (Figure 3B and 3D). Of the two possible enantiomers of compound **2**, the electron density was best explained by the S-enantiomer, which also allows more extensive van der Walls interactions with domain II and is thus likely to be the most active of the two. However, characterization of the inhibitory activity of compound **2** enantiomers separated would be necessary to confirm this.

Furthermore, IRAP was not in the same conformation in the two structures. In the structure with compound **1**, IRAP was in a closed conformation, virtually identical to the one previously reported in complex with a transition state analogue tripeptide [36], with a root mean square deviation between C-alpha atom position of 0.391 Å. In contrast, in the structure with compound **2**, IRAP was found in a more open conformation, having a r.m.s.d. of 2.096 Å (C-alpha atoms) compared to the structure with compound **1**, primarily due to the relative movement of domain IV away from domain I, with domain III acting as a hinge (Figure 3F). This conformational change creates a ~10 Å additional gap between domains IV and II (Figure 3F). This conformational change is necessary to accommodate compound **2**, since it binds in the interface of domains I and IV, apparently stabilizing this conformation. This "semi-open" conformation highly resembles the conformation that IRAP was crystallized in complex with a 10mer model antigenic peptide precursor (r.m.s.d. of C-alpha atoms between the two structures was 0.542 Å) [34]. In that structure, the interactions between the C-terminal moiety of the peptide and the base of the interface of domain III and IV was hypothesized to stabilize that conformation [34].

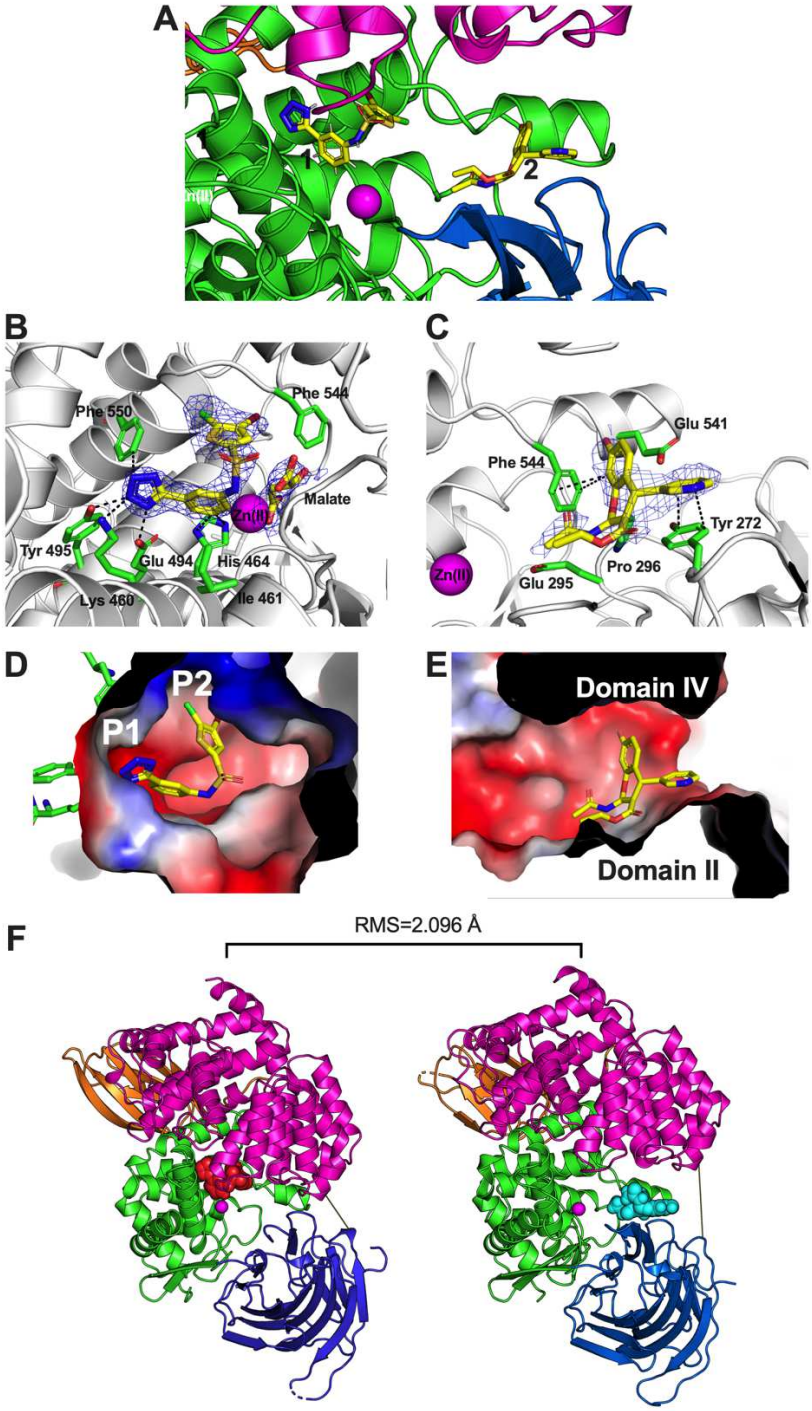

Figure 3: Crystal structures of IRAP in complex with compound **1** and compound **2**. ***Panel A,*** schematic representation of the catalytic site of IRAP indicating the locations of the active site zinc(II) atom and the two compounds indicated by numbers **1** and **2** and shown in stick representation. ***Panels B and C***, Schematic representation of compounds **1** and **2** in complex with IRAP. Compounds are depicted in stick representation colored by atom (carbon = yellow, oxygen = red, nitrogen = blue, sulfur = orange). Blue mesh indicates the $2F_o - F_c$ electron density map contoured at 1.0 sigma (carve = 1.6). IRAP side-chains that come within 4 Å of the inhibitor are shown in stick representation (carbon = green, oxygen = red, nitrogen = blue). The overall structure of IRAP is shown in white cartoon representation.

Dotted lines indicate atomic interactions described in the results section. ***Panels D and E,*** same as in panels A and B, but IRAP is depicted in surface representation colored by electrostatic potential. P1 and P2 indicated pockets that accommodate sidechains of compound **1**. IRAP domains are colored as in panel A. ***Panel F***, cartoon representation of the structures colored by domain (domain I = blue, domain II =green, domain III = gold and domain IV = magenta). Active-site catalytic zinc(II) atom is shown as a magenta sphere. Compound **1** is shown in red sphere representation and compound **2** in light blue spheres. The root mean square deviation between the atoms in each structure is indicated.

The two different conformations of IRAP also differ in the organization of the active site and the S1 specificity pocket (Figure 4). The catalytic residue Tyr549 has been reported before to change orientation depending on the overall conformation of IRAP and to orient to a catalysis-favored configuration in the closed conformation[36]. Accordingly, in the co-crystal structure of IRAP with compound **1**, Tyr549 is oriented toward the active site zinc(II), whereas in the co-crystal structure of IRAP with compound **2**, Tyr549 is facing away in a configuration not fully-optimized with the known catalytic mechanism of IRAP and homologous enzymes like ERAP1 [41]. Similarly, the configuration of the GAMEN motif, a short loop important for catalytic site organization and substrate specificity in M1 aminopeptidases, is dramatically different between the two structures. In the structure with compound **1**, the GAMEN loop adopts a configuration that is essentially identical to the one seen in the closed conformation of IRAP with bound a transition-state analog [36]. This GAMEN loop configuration was hypothesized before to arise due to direct interactions with the transition-state analog but persists here despite the lack of direct interactions with compound **1**. In contrast, in the structure with compound **2**, the GAMEN loop adopts a distinct configuration that is identical to the one seen in the empty IRAP, or in IRAP in complex with a 10mer peptide analog, a configuration that leads to a more open catalytic site. Residue Phe544, previously proposed to be important for compound **2** binding in the active site [42], lines the side of the S1 specificity pocket of the enzyme that is important for the specificity of IRAP for N-terminal amino acids that carry small hydrophobic residues [33–35,43], and is in a similar configuration in all structures, although it does feature a small shift towards compound **2**, resulting in some van der Walls interactions. Strikingly, residue Glu541, a residue that is responsible for the dual specificity of IRAP for both hydrophobic and positively charged amino acids, is in a different orientation in the structure with compound **2**, and faces away from the S1 pocket likely due to steric interactions with the inhibitor (Figure 4). Thus, it appears that part of compound **2**, facing away from the S1

pocket occupies the depth of the S1 specificity pocket of IRAP as this is configured in the open conformation.

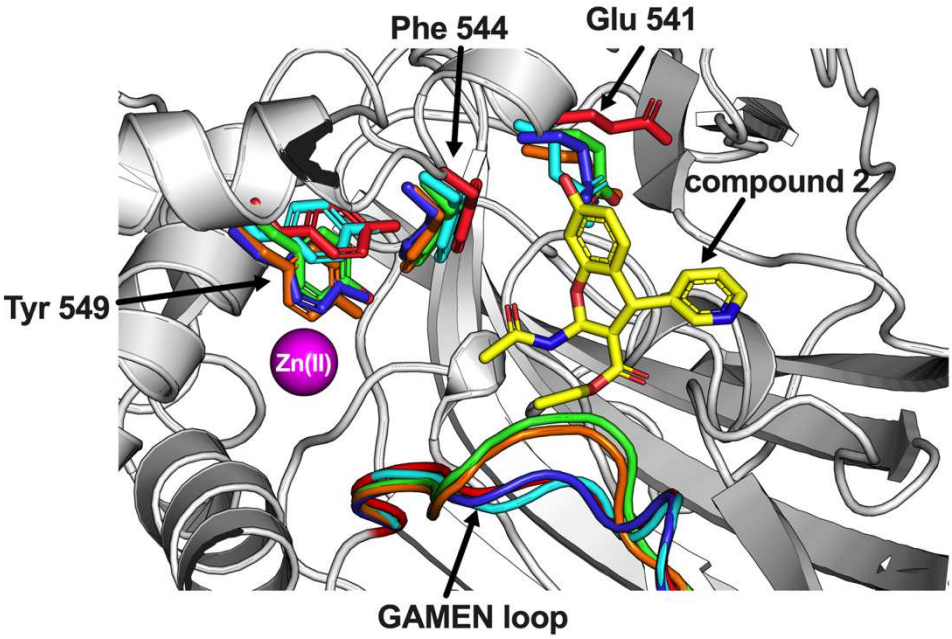

Figure 4: Overlay of crystal structures of the two compounds (compound **1** structure in orange, compound **2** in red) with previously determined structures of empty IRAP (PDB=5C97, in cyan), IRAP in complex with a 10mer peptidic substrate analogue (PDB=4Z7I, in blue) and IRAP in complex with a transition state analogue (PDB= 5MJ6, in green). The catalytic residue Tyr549, the S1 pocket residues Phe544 and Glu541 and the GAMEN loop are indicated.

*Compound **1** induces a more closed IRAP conformation in solution than compound **2***

To confirm that the substantial conformational alteration between IRAP bound to compound **1** and compound **2** observed in the crystal structures reflected actual differences in solution and not crystal packing effects or differences between the crystallization solutions, we examined the solution structures of the inhibited complexes using small-angle X-ray scattering (SAXS). Samples of IRAP (5-15 μM) containing compound **1** or compound **2** (40μM) in a physiological salt solution at pH 7.2 were analyzed. Under these conditions, the enzyme is expected to be >99% occupied by inhibitor. Guinier analysis revealed a significant difference between the radius of gyration (R_g) for the two complexes, with radius of gyration (R_g) for IRAP bound to compound **1** 4.5Å smaller than for IRAP bound to compound **2** (Figure 5). These data show that, in solution, compound **1** induces a substantially more compact structure than compound **2**, consistent with the crystallographic analysis.

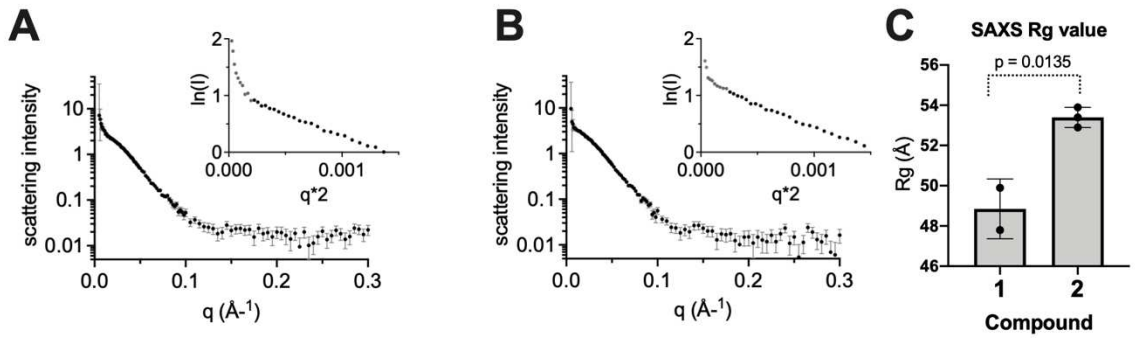

Figure 5: Solution small-angle X-ray scattering of IRAP bound to compounds **1** and **2**. **Panels A and B**; Scattering profiles with insets showing Guiner plots. **Panel C;** R_g values calculated from slope of Guinier plot in the linear range for two (compound **1**) or three (compound **2**) samples, p-value from unpaired t-test.

Inhibition of oxytocin cleavage

The observation that compound **2** acts as an uncompetitive inhibitor and binds in an allosteric site prompted us to examine its potency in inhibiting a more physiological substrate for IRAP, the macrocyclic peptidic hormone oxytocin (Figure 6A). Typical textbook uncompetitive inhibition is considered to arise when the inhibitor interacts only with the enzyme-substrate complex, suggesting that the interaction can be substrate specific. Since the typical fluorogenic substrate used to discover and characterize IRAP inhibitors is dipeptidic in nature, it is important to confirm inhibition with larger, more physiologically-relevant substrates. Toward this, we utilized a recently developed *in vitro* assay, in which oxytocin cleavage is followed by high-performance liquid chromatography [44](Figure 6B). Incubation of oxytocin with IRAP leads to the generation of trimming products that is completely inhibited in the presence of the transition-state analogue DG026, a compound shown by x-ray crystallography to bind in a substrate-like orientation in the active site [36]. The presence of compound **1** in the reaction mixture at a concentration 10-fold over the IC_{50} value calculated for the dipeptidic substrate, reduced the amount of trimming products produced significantly. In contrast, the inclusion of compound **2** in the mixture at a concentration of 10-fold over the IC_{50} value calculated for the dipeptidic substrate L-AMC, did not have any observable inhibitory effect (Figure 6C). To confirm this result, we performed a titration using this assay for both compounds and calculated IC_{50} values for the ability of the compounds to inhibit the degradation of oxytocin (Figure 6D). Compound **1** was found to be able to fully inhibit oxytocin cleavage with an IC_{50} of 2.5 µM, which is 10-fold higher compared to the small substrate. In contrast, compound **2**, was found to be a

very poor inhibitor of oxytocin cleavage by IRAP, with a calculated IC_{50} of over 200 μM, which is >500-fold weaker compared to the potency of this inhibitor versus the dipeptidic substrate. Thus, although the inhibitory potency of compound **1** largely translates to the larger substrate, this does not apply for compound **2** which fails to effectively inhibit the cleavage of oxytocin by IRAP.

To confirm these surprising results, we utilized an orthogonal enzymatic assay in which the detection of the peptidic products is performed by MALDI-MS. A similar assay has been used before for the study of peptide trimming by the homologous aminopeptidase ERAP1 [45]. MALDI-MS analysis successfully identified the MW of oxytocin at 1007.42 daltons and the product of the cleavage of the N-terminal peptide bond at 1025.43 (Figure 6E and Supporting Figure S2). This cleavage would result in linearization of oxytocin which would block its biological functions. No further trimming of oxytocin was evident under these conditions. Kinetic analysis revealed the reduction of the substrate peak upon incubation with enzyme (Figure 6E, top) which was inhibited by compound **1** (Figure 5E, bottom left) but not by compound **2** (Figure 5E, bottom right).

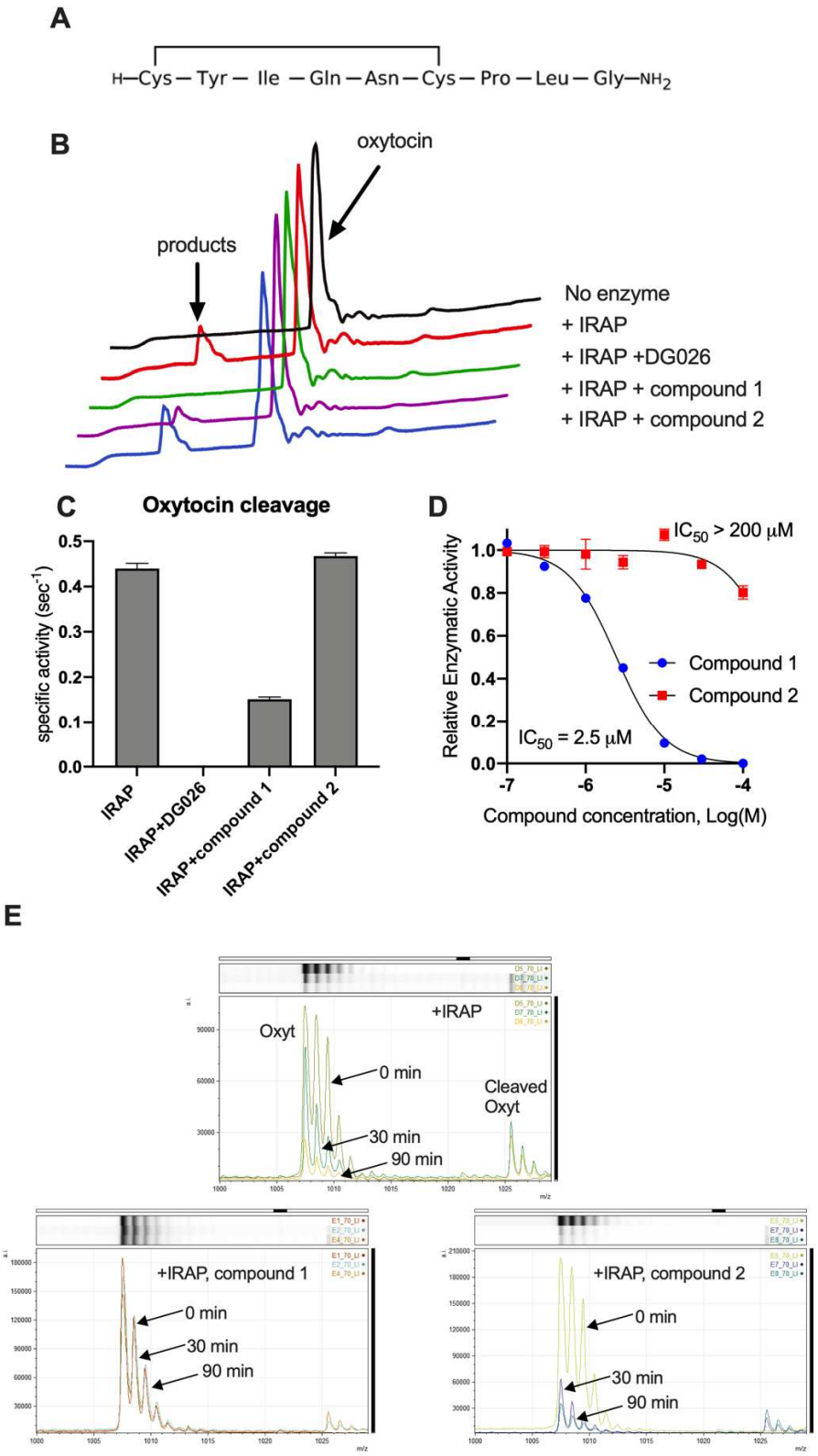

Figure 6: Panel A, Amino acid sequence of oxytocin. **Panel B,** representative HPLC traces of oxytocin and oxytocin incubated with 10 nM IRAP for 30 min at 37°C in the presence or absence of inhibitor DG026 and compound **1** or **2**. The peak of oxytocin and digestion products are indicated. **Panel C,** calculated specific activity of oxytocin digestion by IRAP in the presence or absence of inhibitors. No detectable products were found in the presence of DG026 and thus the specific activity was plotted to be zero. **Panel D,** effect of titration of

compound **1** and **2** on the digestion of oxytocin by IRAP. Data were fit to a variable slope log(inhibitor) versus response model using GraphPad Prism 8.0 to calculate the IC_{50} values indicated in the graph. **Panel E,** MALDI-MS spectra of oxytocin incubated with IRAP in the presence or absence of compound **1** or compound **2.** Time points are indicated in each graph. The reduction in peak intensity of oxytocin was used to follow inhibition of IRAP by each compound.

The inability of compound **2** to efficiently inhibit the degradation of oxytocin by IRAP may suggest that oxytocin and compound **2** can concurrently bind IRAP without compound **2** blocking catalysis. Unfortunately, no crystal structure of IRAP in complex with oxytocin has been reported. As a surrogate, we modelled the structure of a 10mer peptide analog DG025, which binds in the same open conformation of IRAP that compound **2** also binds [34]. In the DG025-IRAP co-crystal structure, the S1 pocket of IRAP is occupied by a homophenylalanine side-chain. Oxytocin has a cysteine residue at the equivalent position that participates in an internal disulfide bond to stabilize its macrocyclic nature. We, therefore, modelled IRAP bound to a DG025 variant that carries a cysteine residue at its N-terminal position and assessed whether this variant could concurrently bind IRAP with compound **2**. Indeed, no steric interaction was evident between the two molecules, although the closest atoms approach at ~3Å (Figure 7). This observation suggests that a peptide with a small residue at its N-terminus may be able to be cleaved by IRAP even in the presence of compound **2** and forms a useful framework for understanding the inability of compound **2** to inhibit efficiently oxytocin cleavage by IRAP.

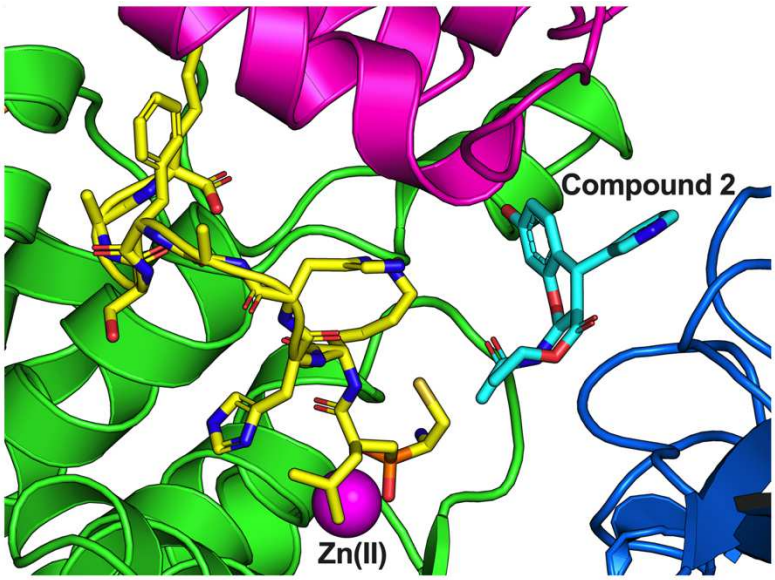

Figure 7: Schematic representation of a model of the peptide analogue DG025 in which the N-terminal amino acid was replaced by a cysteine residue, bound in IRAP adjacent to compound **2**. The peptide was modelled at the exact orientation found in the co-crystal structure of IRAP (PDB code=4Z7I) and compound **2** in the orientation found in the crystal structure described in this manuscript. IRAP domains are colored as in Figure 1. No steric clashes are found between the two compounds.

DISCUSSION

Inhibition of physiological substrates

In our effort to better understand the mechanism of action of two common IRAP inhibitors, we discovered that one of them presented unexpected kinetic behavior. Indeed, although compound **2** is a potent inhibitor for a small dipeptidic fluorogenic substrate, it does not inhibit the cleavage of a larger cyclic peptide which is a major physiological substrate for this enzyme. This finding acts as a cautionary tale for due diligence in inhibitor characterization during drug discovery efforts and highlights how multiple enzyme conformations can complicate drug discovery. Compound **2** has been used extensively in the literature and is commercially available as an IRAP inhibitor. Its inability, however, to inhibit a physiologically relevant substrate directly suggests that previous experimental interpretations of compound **2** activity in cellular or *in vivo* contexts may need to be re-evaluated. Although our results do not dispute that compound **2** has a direct pharmacological effect on IRAP, they suggest that the exact nature of this effect may be substrate-dependent. This would be of critical importance for *in vivo* evaluations in which the physiological substrate of IRAP is not always clear or even known. Thus previous *in vivo* effects of compound **2** may need to be validated by additional IRAP inhibitors that utilize different mechanisms of action.

Furthermore, the finding that both compounds analyzed here, discovered by random screening campaigns, do not engage the active site zinc(II) but rather proximal allosteric sites, suggests that IRAP is amenable to complex mechanisms of modulation that can be substrate-specific. This is both a nuisance and an opportunity. Although it suggests that detailed mechanistic analysis of IRAP inhibitors is crucial before assuming activity versus physiological substrates *in vivo*, at the same time affords opportunities for targeting specific biological functions of this enzyme.

Mechanism of inhibition and substrate dependency

Combining enzymatic with structural analysis can help us put forward a mechanistic model of IRAP inhibition that considers both conformations of the enzyme (Figure 8). According to this model IRAP cycles between two main conformations: one open and one closed. Both conformations can lead to substrate turnover, although in the closed conformation the optimal orientation of the catalytic site tyrosine (Tyr549) and GAMEN motif results in much faster catalysis. A small substrate like L-AMC can be hydrolyzed by both conformations but its hydrolysis rate is dominated by the closed conformation. In contrast, larger peptidic substrates must be processed by the open conformation because their C-terminal moiety does not allow domain closure. Although large substrate turnover would be expected to proceed slowly, the additional interactions provided by the full length of the substrate can enhance K_M, leading to appreciable catalytic rates under physiological conditions.

According to this model, an inhibitor like compound **1** (I_1 in Figure 8) can bind to the closed conformation, thus shifting the equilibrium to the closed state. Compound **1** can form non-product complexes with both ES and E, thus behaving as a non-competitive inhibitor. Furthermore, compound **1** inhibits the turnover of large substrates by either promoting the closed conformation, which is unable to bind a large substrate, or by direct steric clashes that preclude substrate binding.

In contrast to compound **1**, compound **2** (I_2 in Figure 8), binds only to the open conformation of the enzyme since its binding site is only formed in that conformation. While a small substrate may still be able to bind and be hydrolyzed, its turnover rate would be greatly reduced due to the unoptimized positions of catalytic residues in that conformation, thus leading to an apparent reduction of the k_{cat} which would make the inhibitor display an uncompetitive mechanism. In contrast, a large substrate that is normally hydrolyzed by the open conformation would not be affected by this inhibitor.

An alternative explanation could consider an additional conformational state of IRAP specialising in large substrates like oxytocin. Indeed, a significantly more open conformation has been observed both in crystals and in solution for the highly homologous ERAP1, an enzyme optimized in trimming large antigenic peptide precursors [46] and also postulated by molecular dynamics calculations for IRAP [47]. If large cyclic peptides like oxytocin are

preferably processed by such an open state of IRAP, the larger distance between domains IV and II would *de facto* eradicate the compound **2** binding site. However, such a mechanism is not obligatory to explain the behaviour observed here.

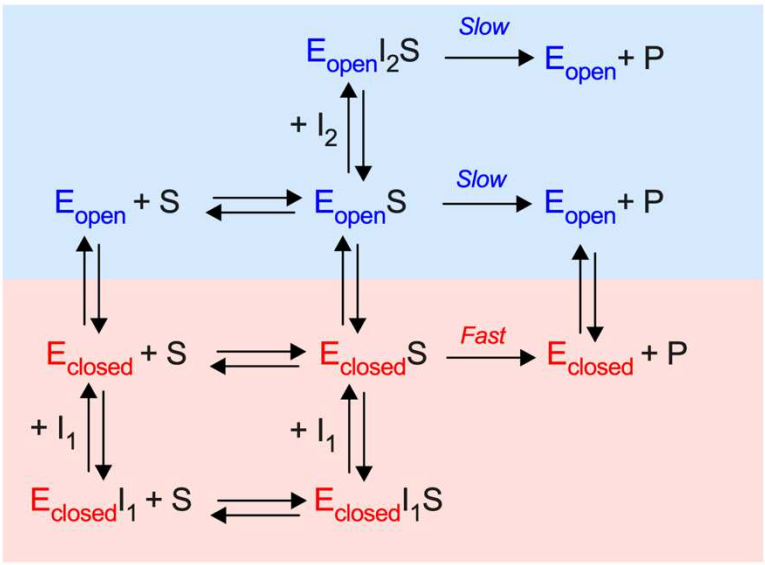

Figure 8: Kinetic model of IRAP enzymatic mechanism. IRAP can access two conformations ("open" and "closed") of which the closed conformation has an optimized catalytic center that allows for fast conversion of substrate to product. Small substrates such as L-AMC can access both conformations, but it is rapidly turned over by the closed conformation. Large substrates such as DG025 or oxytocin can only bind to the open conformation and are turned over more slowly. Compound **1** (I_1) can bind to the closed conformation and block catalytic turnover, thus acting as a non-competitive inhibitor. Compound **2** (I_2) binds only to the open conformation but still allows catalytic turnover. Small substrates are thus limited to the slow pathway which results in an apparent k_{cat} reduction whereas large substrates that already use this pathway anyway are mostly unaffected.

Conformational changes as a central component of enzyme function and inhibition

Our findings highlight that IRAP conformational changes are a central component of enzyme function and determine interactions and selectivity for both substrates as well as inhibitors. In this context, complex or unusual inhibition mechanisms may be more common for this enzyme than previously thought and even active-site inhibitors that target distinct conformations may appear non-competitive, as demonstrated in similar systems [48,49], necessitating a careful combination of both kinetic and structural analysis for any new drug lead for this enzyme. Furthermore, the mechanism of inhibition proposed here is reminiscent of the mechanism proposed for the homologous enzyme ERAP1 with some marked differences [50][46]. ERAP1 appears to feature more wide-open conformations in

both crystals and in solution and to be able to accommodate large peptides inside the substrate cavity even in the closed conformation. IRAP appears to be more conformational restricted in terms of the overall breadth of conformational change but at the same time displays greater plasticity in the catalytic site and in particular the GAMEN motif [36]. The unique selectivity of compound **2** for both a particular conformation and a particular substrate suggests some degree of substrate specialization for different conformations, which could be exploited to generate or optimize substrate-selective inhibitors for this enzyme. This could have an important pharmacological impact since the multitude of biological functions of IRAP limits its clinical value as a drug target and the ability to inhibit processing of specific substrates (and thus biological functions) could provide an elegant solution to this limitation. In addition, targeting allosteric sites of enzymes can be advantageous for selectivity purposes since these allosteric sites are usually not conserved amongst other family members, whereas the active site is highly conserved. Indeed, this has been demonstrated for the highly homologous enzyme ERAP1[51,52]. Given the discovery that these two common IRAP inhibitors are allosteric, these compounds can now constitute novel starting points for the optimization of inhibitor properties in the context of potency, selectivity, and substrate-specificity.

In summary, we have characterized two inhibitors of IRAP, an enzyme with important biological functions that is an emerging target for pharmacological approaches. Using enzymological and structural approaches we discovered that although these compounds were considered to target the catalytic site of the enzyme, they are in contrast, allosteric, and can be substrate-specific, by stabilizing distinct conformations of the enzyme. Our results highlight the importance of conformational rearrangements in the IRAP enzymatic mechanism, and that allosteric inhibition may constitute an advantageous approach for substrate-selective modulation of IRAP function.

EXPERIMENTAL PROCEDURES

Recombinant Enzyme

Recombinant IRAP used for enzymatic assays and for crystallization was expressed and purified as previously described [36]. Briefly, the extracellular enzymatic domain of IRAP was expressed by stably-transfected HEK 293S GnTI$^{(-)}$ cells and purified by affinity

chromatography. For crystallization experiments, the protein was additionally purified by size-exclusion chromatography (Superdex 200 16/60 column; GE Healthcare™) and the peak corresponding to the native IRAP dimer was concentrated by ultrafiltration. For the enzymatic assays the recombinant protein was stored in the presence of 10% glycerol at -80 °C until needed.

Fluorogenic assay

For determination of inhibitor potency and Michaelis-Menten analysis, the activity of the enzyme was calculated by measuring the rate of hydrolysis of the model fluorogenic substrate L-leucine-7-amido-4-methyl coumarin (L-AMC, Sigma–Aldrich, L2145) followed at 460 nm (excitation at 380 nm) using a Spark 10M (TECAN) multimode microplate reader as previously described [53]. For calculation of the *in vitro* IC_{50} values, experimental data were fit to a four-parameter inhibitor versus response model using Graphpad Prism 8.0. For Michaelis-Menten analysis, initial reaction rates were calculated for each concentration of substrate and the data were fit to a classical Michaelis-Menten model using Graphpad Prism 8.0.

Oxytocin cleavage assay

Oxytocin cleavage by IRAP was followed by high-performance liquid chromatography as described before [44]. Briefly, 40 µM oxytocin was incubated with 10 nM recombinant IRAP at 37◦C for 30 min and the reaction was terminated by adding 0.25% (v/v) trifluoroacetic acid (TFA) and stored at –80 °C until analysis. The reactions were analyzed using a reversed-phase C18 column (chromolith C-18 column, Merck, Kenilworth, NJ, USA) using a linear gradient (solvent A: 0.05% TFA, 10% acetonitrile, solvent B: 0.05% TFA, 50% acetonitrile). The surface of the peak corresponding to the digestion products was compared to a control reaction to evaluate inhibition efficiency.

Oxytocin cleavage was also followed by MALDI-MS. For this assay, 100 µM oxytocin was incubated with 30 nM recombinant IRAP in the absence or the presence of 2.5 µM of compound **1** or 4.8 µM compound **2**, at 37°C for 90 min. The reactions were terminated by the addition of TFA at a final concentration of 0.1% (v/v). Measurements were performed using a Bruker microflex LRF MALDI TOF mass spectrometer (Bruker Daltonics, Bremen, Germany), in positive ionization, reflector mode, and an m/z detection range of 0.5 to 1.2

kDa. The samples were mixed with the matrix solution (sinapinic acid saturated in TA30 solvent) in equal volumes and spotted on a Ground Steel (MSP-96) target plate. Protein Calibration Standard I (Bruker Daltonics, Bremen, Germany) was used for the external and internal mass calibration. FlexControl 3.4 (Bruker Daltonics, Bremen, Germany) and flexAnalysis 3.4 (Bruker Daltonics, Bremen, Germany) software were used for instrument control and for post-processing, respectively.

Crystallization and data collection

Crystals of IRAP complexes with the two compounds were obtained after screening using the commercially available PACT-premier crystallization screen (Molecular Dimensions™). Crystals were grown at 16°C by the sitting-drop vapor-diffusion method in 0.1 M MMT buffer (Malic acid, MES, Tris), pH 5.0 and 25% (w/v) polyethylene glycol (PEG) of mean M.W 1500 (D2 condition PACT) for compound **1** and 0.1M SPG buffer (Succinic acid, Phosphate, Glycine), pH 9.0 and 25% (w/v) polyethylene glycol (PEG) (A6 condition PACT) for compound **2**. One hour before crystallization tests, purified IRAP at 9.8 mg/ml was mixed with each compound at a molar ratio of 1:5 and the mixture was incubated at 4°C for one hour. Cryoprotection was performed by rapid immersion in a solution containing the precipitant and 20% ethylene glycol for 5-10 seconds and then crystals were flash-frozen in liquid N_2. The frozen crystals were shipped in a Taylor-Wharton CX100 dry shipper to the Synchrotron facility. Diffraction datasets were collected at 100 K at a wavelength of 0.976 Å on beamline P13 of Petra III, EMBL, Hamburg, Germany. The reflections were integrated with XDS, the space group was determined with POINTLESS and the data merging was performed with STARANISO. The best dataset for compound **1** displayed diffraction to 2.6 Å and space group P 1 21 1 with a=73.443 Å, b=119.074, c=141.643 Å, and β=102.766 °. For compound **2**, the best dataset had data to 2.8 Å, but after setting as cutoff the value of 50% for CC1/2 and of 1.0 for mean(I/σI) in combination with the percentage of data completeness, the high-resolution limit was finally set at 3.03 Å and the crystals belonged to space group P 1 21 1 with a=68.377 Å, b=257.679, c=73.494 Å, and β=110.444 °.

Structure determination and refinement

Both structures were solved by molecular replacement with PHASER using as a search model the structure of IRAP with PDB ID: 5MJ6 for compound **1** and the structure of

IRAP with PDB ID: 4Z7I for compound **2**. In both cases, two protein molecules were found in the asymmetric unit (referred to as chains A and B). Electron density that was not attributable to the protein molecule was found in each set and interpreted to belong to the bound ligands. For compound **1**, one ligand was identified in each chain, while for compound **2** significant additional density was clear only in chain A. In the structure of IRAP with compound **1**, small additional density adjacent to the catalytic zinc(ii) atom, was interpreted to belong to a molecule of malic acid that was a component of the crystallization mother liquor. Structure refinement was conducted with PHENIX using restrained refinement and non-crystallographic symmetry restraints, while at the final stages TLS refinement was included. Model building and real space refinement were performed in Coot. The structure of IRAP in complex with compound **1** converged to R and R_{free} of 16.92 and 23.13%, respectively. For compound **2**, the R and R_{free} values are 20.31% and 24.19%. For the structure in complex with compound **1**, in chain A, no density was visible before residue 158 and between residues 224-226 and 639-648 while in chain B, no density was visible before residue 159 and between residues 224-225 and 641-647. The model also includes 45 molecules of N-acetyl-D-glucosamine, 10 molecules Beta-D-mannose, 12 molecules alpha-D-mannopyranose, 2 molecules malic acid, 2 polyethylene glycols, 3 molecules 1,2-Ethanediol as well as 190 water molecules. Accordingly, for the structure in complex with compound **2**, in chain A, no density was visible before residue 160 and between residues 641-647 and 662-664 while in chain B, no density was visible before residue 159 and between residues 224-228, 640-645 and 662. The final model also includes 35 molecules N-acetyl-D-glucosamine, 8 molecules Beta-D-mannose, 5 molecules alpha-D-mannopyranose, 1 polyethylene glycol, 2 molecules 1,2-Ethanediol 4 glycine residues and 72 water molecules.

Small-angle X-ray Scattering

SAXS data were collected using at the National Synchrotron Light Source-II LiX beamline [53] using a mail-in protocol [54]. IRAP samples were freshly prepared as described above, with the final gel filtration step performed the day before SAXS analysis. Peak fractions in phosphate-buffered saline (137 mM NaCl, 2.7 mM KCl, 12 mM phosphate buffer pH 7.4) were collected and placed on ice. Concentrated compound **1** or compound **2** in DMSO was added, and the mixture was concentrated by ultrafiltration as described

above, reserving both concentrate and filtrate. Three samples of IRAP at concentrations of 1.5, 1.0, and 0.5 mg/ml containing 40 μM inhibitor were prepared by mixing concentrate and filtrate in different ratios. The samples, along with inhibitor-containing ultrafiltrate-only buffer controls, were shipped at ~4 °C to NSLSII for data collection the next day. Parallel samples stored at 4°C did not exhibit detectable aggregation over the course of 5 days. Scattering curves were collected using 0.8249Å radiation, and background was subtracted using matched and scaled buffer control scattering curves [55]. Guinier plot R_g calculations were performed using ATSAS 3.0 [56].

Author Contributions

A.M. produced and purified recombinant enzymes, performed enzymatic analysis, analyzed and interpreted data, crystallized the proteins, and solved the crystal structures. P.G. helped with protein crystallization, performed x-ray diffraction experiments, and analyzed x-ray diffraction data. K.R. and L.L. produced and purified recombinant IRAP for SAXS analysis. L.J.S. performed the SAXS analysis. I.B. performed the mass spectrometry analysis and analyzed data with help from A.M. and E.S.. N.T. contributed to the development of the MALDI-MS methodology. E.S. conceived and supervised the project, analyzed and interpreted data, and wrote the manuscript with input from all authors. All authors have approved the final version of the manuscript.

Funding

We acknowledge the support of this work by the project "INSPIRED-The National Research Infrastructures on Integrated Structural Biology, Drug Screening Efforts and Drug Target Functional Characterization" (grant MIS 5002550), which is implemented under the Action "Reinforcement of the Research and Innovation Infrastructure", funded by the Operational Programme "Competitiveness, Entrepreneurship and Innovation" (grant NSRF 2014−2020) and co-financed by Greece and the European Union (European Regional Development Fund) and the US National Institutes of Health (grant R01-AI153828 to LJS). The LiX beamline is part of the Center for BioMolecular Structure (CBMS), which is primarily supported by the National Institutes of Health, National Institute of General Medical Sciences (NIGMS) through a P30 Grant (P30GM133893), and by the DOE Office of Biological and Environmental Research (KP1605010). LiX also received additional support from NIH

Grant S10 OD012331. As part of NSLS-II, a national user facility at Brookhaven National Laboratory, work performed at the CBMS is supported in part by the U.S. Department of Energy, Office of Science, Office of Basic Energy Sciences Program under contract number DE-SC0012704. The authors would also like to acknowledge financial support by Pharmaxis Ltd.

Acknowledgments

We thank the beamline scientists of EMBL-Hamburg for their assistance during data collection at the P13 beamline of Petra III, Hamburg, Germany. We thank Dr. Shrirish Chodankar and the beamline staff for assistance with data collection at the LiX beamline of NSLSII, Brookhaven, NY, USA. The authors would like to thank Pharmaxis Ltd and specifically Drs Dieter Hamprecht and Alison Findlay for providing the compounds used in this study and for helpful discussions.

Conflict of interest

The authors declare no competing financial interest.

Data deposition

Atomic coordinates and structure factors have been deposited in the Protein Data Bank (https://www.rcsb.org/) with PDB codes 8CGP for compound **1** and 8CGW for compound **2**.

Accession Numbers:

PDB ID: 8CGP

PDB ID: 8CGW

REFERENCES

1. Tsujimoto, M.; Hattori, A. The oxytocinase subfamily of M1 aminopeptidases. *Biochim Biophys Acta* **2005**, *1751*, 9–18.
2. Keller, S.R. The insulin-regulated aminopeptidase: a companion and regulator of GLUT4. *Front Biosci* **2003**, *8*, s410-20.
3. Tsujimoto, M.; Mizutani, S.; Adachi, H.; Kimura, M.; Nakazato, H.; Tomoda, Y. Identification of human placental leucine aminopeptidase as oxytocinase. *Arch. Biochem. Biophys.* **1992**, *292*, 388–392, doi:10.1016/0003-9861(92)90007-J.
4. Saveanu, L. IRAP Identifies an Endosomal Compartment Required for MHC Class I Cross-Presentation. *Science (80-.).* **2009**, *325*, 213–217, doi:10.1126/science.1172845.
5. Evnouchidou, I.; Chappert, P.; Benadda, S.; Zucchetti, A.; Weimershaus, M.; Bens, M.; Caillens, V.; Koumantou, D.; Lotersztajn, S.; van Endert, P.; et al. IRAP-dependent endosomal T cell receptor signalling is essential for T cell responses. *Nat. Commun.* **2020**, *11*, doi:10.1038/s41467-020-16471-7.
6. Ascher, D.B.; Cromer, B.A.; Morton, C.J.; Volitakis, I.; Cherny, R.A.; Albiston, A.L.; Chai, S.Y.; Parker, M.W. Regulation Of Insulin-Regulated Membrane Aminopeptidase Activity By Its C-terminal Domain. *Biochemistry* **2011**, doi:10.1021/bi101893w.
7. Bernstein, H.G.; Müller, S.; Dobrowolny, H.; Wolke, C.; Lendeckel, U.; Bukowska, A.; Keilhoff, G.; Becker, A.; Trübner, K.; Steiner, J.; et al. Insulin-regulated aminopeptidase immunoreactivity is abundantly present in human hypothalamus and posterior pituitary gland, with reduced expression in paraventricular and suprachiasmatic neurons in chronic schizophrenia. *Eur. Arch. Psychiatry Clin. Neurosci.* **2017**, *267*, 427–443, doi:10.1007/s00406-016-0757-7.
8. Saveanu, L.; Carroll, O.; Weimershaus, M.; Guermonprez, P.; Firat, E.; Lindo, V.; Greer, F.; Davoust, J.; Kratzer, R.; Keller, S.R.; et al. IRAP Identifies an Endosomal Compartment Required for MHC Class I Cross-Presentation. *Science (80-.).* **2009**, *325*, 213–217.
9. Herbst, J.J.; Ross, S.A.; Scott, H.M.; Bobin, S.A.; Morris, N.J.; Lienhard, G.E.; Keller, S.R. Insulin stimulates cell surface aminopeptidase activity toward vasopressin in adipocytes. *Am J Physiol* **1997**, *272*, E600-6, doi:10.1152/ajpendo.1997.272.4.E600.
10. Chai, S.Y.; Yeatman, H.R.; Parker, M.W.; Ascher, D.B.; Thompson, P.E.; Mulvey, H.T.; Albiston, A.L. Development of cognitive enhancers based on inhibition of insulin-regulated aminopeptidase. *BMC Neurosci.* **2008**, *9 Suppl 2*, S14, doi:10.1186/1471-2202-9-S2-S14.
11. Barlow, N.; Thompson, P.E. IRAP Inhibitors: M1-Aminopeptidase Family Inspiration. *Front. Pharmacol.* 2020, *11*.
12. Pham, V.; Albiston, A.L.; Downes, C.E.; Wong, C.H.; Diwakarla, S.; Ng, L.; Lee, S.; Crack, P.J.; Chai, S.Y. Insulin-regulated aminopeptidase deficiency provides protection against ischemic stroke in mice. *J Neurotrauma* **2012**, *29*, 1243–1248, doi:10.1089/neu.2011.1824.
13. Andersson, H.; Hallberg, M. Discovery of inhibitors of insulin-regulated aminopeptidase as cognitive enhancers. *Int J Hypertens* **2012**, *2012*, 789671, doi:10.1155/2012/789671.
14. Diwakarla, S.; Nylander, E.; Gronbladh, A.; Vanga, S.R.; Khan, Y.S.; Gutierrez-de-Teran,

H.; Savmarker, J.; Ng, L.; Pham, V.; Lundback, T.; et al. Aryl Sulfonamide Inhibitors of Insulin-Regulated Aminopeptidase Enhance Spine Density in Primary Hippocampal Neuron Cultures. *ACS Chem Neurosci* **2016**, *7*, 1383–1392, doi:10.1021/acschemneuro.6b00146.

15. de Villiers, W.J.; van der Westhuyzen, D.R.; Coetzee, G.A.; Henderson, H.E.; Marais, A.D. The apolipoprotein E2 (Arg145Cys) mutation causes autosomal dominant type III hyperlipoproteinemia with incomplete penetrance. *Arterioscler. Thromb. Vasc. Biol.* **1997**, *17*, 865–872.
16. Telianidis, J.; Hunter, A.; Widdop, R.; Kemp-Harper, B.; Pham, V.; McCarthy, C.; Chai, S.Y. Inhibition of insulin-regulated aminopeptidase confers neuroprotection in a conscious model of ischemic stroke. *Sci. Reports 2023 131* **2023**, *13*, 1–17, doi:10.1038/s41598-023-46072-5.
17. Vear, A.; Gaspari, T.; Thompson, P.; Chai, S.Y. Is There an Interplay Between the Functional Domains of IRAP? *Front. Cell Dev. Biol.* **2020**, *8*, 1028, doi:10.3389/fcell.2020.585237.
18. Trocmé, C.; Gonnet, N.; Di Tommaso, M.; Samouda, H.; Cracowski, J.-L.; Cracowski, C.; Lambert-Porcheron, S.; Laville, M.; Nobécourt, E.; Gaddhab, C.; et al. Serum IRAP, a Novel Direct Biomarker of Prediabetes and Type 2 Diabetes? *Front. Mol. Biosci.* **2021**, *7*, 596141, doi:10.3389/fmolb.2020.596141.
19. Weglarz-Tomczak, E.; Vassiliou, S.; Mucha, A. Discovery of potent and selective inhibitors of human aminopeptidases ERAP1 and ERAP2 by screening libraries of phosphorus-containing amino acid and dipeptide analogues. *Bioorganic Med. Chem. Lett.* **2016**, *26*, 4122–4126, doi:10.1016/j.bmcl.2016.06.062.
20. Kokkala, P.; Mpakali, A.; Mauvais, F.-X.; Papakyriakou, A.; Daskalaki, I.; Petropoulou, I.; Kavvalou, S.; Papathanasopoulou, M.; Agrotis, S.; Fonsou, T.-M.; et al. Optimization and Structure-Activity Relationships of Phosphinic Pseudotripeptide Inhibitors of Aminopeptidases That Generate Antigenic Peptides. *J. Med. Chem.* **2016**, *59*, 9107–9123, doi:10.1021/acs.jmedchem.6b01031.
21. Papakyriakou, A.; Zervoudi, E.; Tsoukalidou, S.; Mauvais, F.X.; Sfyroera, G.; Mastellos, D.C.; Van Endert, P.; Theodorakis, E.A.; Vourloumis, D.; Stratikos, E. 3,4-diaminobenzoic acid derivatives as inhibitors of the oxytocinase subfamily of m1 aminopeptidases with immune-regulating properties. *J. Med. Chem.* **2015**, doi:10.1021/jm501867s.
22. Andersson, H.; Demaegdt, H.; Vauquelin, G.; Lindeberg, G.; Karlén, A.; Hallberg, M.; Erdélyi, M.; Hallberg, A. Disulfide cyclized tripeptide analogues of angiotensin IV as potent and selective inhibitors of insulin-regulated aminopeptidase (IRAP). *J. Med. Chem.* **2010**, *53*, 8059–8071, doi:10.1021/jm100793t.
23. Albiston, A.L.; Diwakarla, S.; Fernando, R.N.; Mountford, S.J.; Yeatman, H.R.; Morgan, B.; Pham, V.; Holien, J.K.; Parker, M.W.; Thompson, P.E.; et al. Identification and development of specific inhibitors for insulin-regulated aminopeptidase as a new class of cognitive enhancers. *Br. J. Pharmacol.* **2011**, *164*, 37–47, doi:10.1111/j.1476-5381.2011.01402.x.
24. Mountford, S.J.; Albiston, A.L.; Charman, W.N.; Ng, L.; Holien, J.K.; Parker, M.W.; Nicolazzo, J.A.; Thompson, P.E.; Chai, S.Y. Synthesis, structure-activity relationships and brain uptake of a novel series of benzopyran inhibitors of insulin-regulated aminopeptidase. *J Med Chem* **2014**, *57*, 1368–1377, doi:10.1021/jm401540f.
25. Borhade, S.R.; Rosenström, U.; Sävmarker, J.; Lundbäck, T.; Jenmalm-Jensen, A.;

Sigmundsson, K.; Axelsson, H.; Svensson, F.; Konda, V.; Sköld, C.; et al. Inhibition of insulin-regulated aminopeptidase (IRAP) by arylsulfonamides. *ChemistryOpen* **2014**, *3*, 256–263, doi:10.1002/open.201402027.
26. Seyer, B.; Diwakarla, S.; Burns, P.; Hallberg, A.; Grönbladh, A.; Hallberg, M.; Chai, S.Y. Insulin-regulated aminopeptidase inhibitor-mediated increases in dendritic spine density are facilitated by glucose uptake. *J. Neurochem.* **2020**, *153*, 485–494, doi:10.1111/JNC.14880.
27. El-Hawli, A.; Qaradakhi, T.; Hayes, A.; Rybalka, E.; Smith, R.; Caprnda, M.; Opatrilova, R.; Gazdikova, K.; Benckova, M.; Kruzliak, P.; et al. IRAP inhibition using HFI419 prevents moderate to severe acetylcholine mediated vasoconstriction in a rabbit model. *Biomed Pharmacother* **2017**, *86*, 23–26, doi:10.1016/j.biopha.2016.11.142.
28. Krskova, K.; Balazova, L.; Dobrocsyova, V.; Olszanecki, R.; Suski, M.; Chai, S.Y.; Zorad, Š. Insulin-Regulated Aminopeptidase Inhibition Ameliorates Metabolism in Obese Zucker Rats. *Front. Mol. Biosci.* **2020**, *7*, 383, doi:10.3389/fmolb.2020.586225.
29. Albiston, A.L.; Cacador, M.; Sinnayah, P.; Burns, P.; Chai, S.Y. Insulin-regulated aminopeptidase inhibitors do not alter glucose handling in normal and diabetic rats. *J Mol Endocrinol* **2017**, *58*, 193–198, doi:10.1530/JME-17-0033.
30. Wilson, R.E.; Jaquins-Gerstl, A.; Chen, J.; Rerick, M.; Weber, S.G. Electroosmotic Perfusion-Microdialysis Probe Created by Direct Laser Writing for Quantitative Assessment of Leucine Enkephalin Hydrolysis by Insulin-Regulated Aminopeptidase in Vivo. *Anal. Chem.* **2020**, *92*, 14558–14567, doi:10.1021/ACS.ANALCHEM.0C02799.
31. Vanga, S.R.; Åqvist, J.; Hallberg, A.; Gutiérrez De Teran, H. Structural Basis of Inhibition of Human Insulin-Regulated Aminopeptidase (IRAP) by benzopyran-based inhibitors. *Front. Mol. Biosci.* **2021**, *8*, 208, doi:10.3389/FMOLB.2021.625274.
32. Vanga, S.R.; Savmarker, J.; Ng, L.; Larhed, M.; Hallberg, M.; Aqvist, J.; Hallberg, A.; Chai, S.Y.; Gutierrez-de-Teran, H. Structural Basis of Inhibition of Human Insulin-Regulated Aminopeptidase (IRAP) by Aryl Sulfonamides. *ACS Omega* **2018**, *3*, 4509–4521, doi:10.1021/acsomega.8b00595.
33. Albiston, A.L.; Pham, V.; Ye, S.; Ng, L.; Lew, R.A.; Thompson, P.E.; Holien, J.K.; Morton, C.J.; Parker, M.W.; Chai, S.Y. Phenylalanine-544 plays a key role in substrate and inhibitor binding by providing a hydrophobic packing point at the active site of insulin-regulated aminopeptidase. *Mol Pharmacol* **2010**, *78*, 600–607, doi:mol.110.065458 [pii]10.1124/mol.110.065458.
34. Mpakali, A.; Saridakis, E.; Harlos, K.; Zhao, Y.; Papakyriakou, A.; Kokkala, P.; Georgiadis, D.; Stratikos, E. Crystal Structure of Insulin-Regulated Aminopeptidase with Bound Substrate Analogue Provides Insight on Antigenic Epitope Precursor Recognition and Processing. *J. Immunol.* **2015**, *195*, 2842–2851, doi:10.4049/jimmunol.1501103.
35. Hermans, S.J.; Ascher, D.B.; Hancock, N.C.; Holien, J.K.; Michell, B.J.; Chai, S.Y.; Morton, C.J.; Parker, M.W. Crystal structure of human insulin-regulated aminopeptidase with specificity for cyclic peptides. *Protein Sci.* **2015**, *24*, 190–199, doi:10.1002/pro.2604.
36. Mpakali, A.; Saridakis, E.; Harlos, K.; Zhao, Y.; Kokkala, P.; Georgiadis, D.; Giastas, P.; Papakyriakou, A.; Stratikos, E. Ligand-Induced Conformational Change of Insulin-Regulated Aminopeptidase: Insights on Catalytic Mechanism and Active Site Plasticity. *J. Med. Chem.* **2017**, *60*, doi:10.1021/acs.jmedchem.6b01890.
37. Mpakali, A.; Saridakis, E.; Giastas, P.; Maben, Z.; Stern, L.J.; Larhed, M.; Hallberg, M.;

Stratikos, E. Structural Basis of Inhibition of Insulin-Regulated Aminopeptidase by a Macrocyclic Peptidic Inhibitor. *ACS Med. Chem. Lett.* **2020**, doi:10.1021/acsmedchemlett.0c00172.

38. Vourloumis, D.; Mavridis, I.; Athanasoulis, A.; Temponeras, I.; Koumantou, D.; Giastas, P.; Mpakali, A.; Magrioti, V.; Leib, J.; Endert, P. Van; et al. Discovery of Selective Nanomolar Inhibitors for Insulin-Regulated Aminopeptidase Based on α-Hydroxy-β-amino Acid Derivatives of Bestatin. *J. Med. Chem.* **2022**, *65*, doi:10.1021/ACS.JMEDCHEM.2C00904.
39. Mpakali, A.; Saridakis, E.; Harlos, K.; Zhao, Y.; Papakyriakou, A.; Kokkala, P.; Georgiadis, D.; Stratikos, E. Crystal structure of insulin-regulated aminopeptidase with bound substrate analogue provides insight on antigenic epitope precursor recognition and processing. *J. Immunol.* **2015**, *195*, doi:10.4049/jimmunol.1501103.
40. Albiston, A.L.; Morton, C.J.; Ng, H.L.; Pham, V.V.; Yeatman, H.R.; Ye, S.; Fernando, R.N.; De Bundel, D.; Ascher, D.B.; Mendelsohn, F.A.O.; et al. Identification and characterization of a new cognitive enhancer based on inhibition of insulin-regulated aminopeptidase. *FASEB J.* **2008**, *22*, 4209–4217, doi:10.1096/fj.08-112227.
41. Kochan, G.; Krojer, T.; Harvey, D.; Fischer, R.; Chen, L.; Vollmar, M.; von Delft, F.; Kavanagh, K.L.; Brown, M.A.; Bowness, P.; et al. Crystal structures of the endoplasmic reticulum aminopeptidase-1 (ERAP1) reveal the molecular basis for N-terminal peptide trimming. *Proc. Natl. Acad. Sci. U. S. A.* **2011**, *108*, 7745–7750, doi:10.1073/pnas.1101262108.
42. Albiston, A.L.; Pham, V.; Ye, S.; Ng, L.; Lew, R. a; Thompson, P.E.; Holien, J.K.; Morton, C.J.; Parker, M.W. Phenylalanine-544 Plays a Key Role in Substrate and Inhibitor Binding by Providing a Hydrophobic Packing Point at the. **2010**, *78*, 600–607, doi:10.1124/mol.110.065458.
43. Zervoudi, E.; Papakyriakou, A.; Georgiadou, D.; Evnouchidou, I.; Gajda, A.; Poreba, M.; Salvesen, G.S.; Drag, M.; Hattori, A.; Swevers, L.; et al. Probing the S1 specificity pocket of the aminopeptidases that generate antigenic peptides. *Biochem. J.* **2011**, *435*, doi:10.1042/BJ20102049.
44. Temponeras, I.; Chiniadis, L.; Papakyriakou, A.; Stratikos, E. Discovery of Selective Inhibitor Leads by Targeting an Allosteric Site in Insulin-Regulated Aminopeptidase. *Pharmaceuticals (Basel).* **2021**, *14*, doi:10.3390/ph14060584.
45. Mavridis, G.; Arya, R.; Domnick, A.; Zoidakis, J.; Makridakis, M.; Vlahou, A.; Mpakali, A.; Lelis, A.; Georgiadis, D.; Tampé, R.; et al. A systematic re-examination of processing of MHCI-bound antigenic peptide precursors by endoplasmic reticulum aminopeptidase 1. *J. Biol. Chem.* **2020**, *295*, 7193–7210, doi:10.1074/jbc.RA120.012976.
46. Maben, Z.; Arya, R.; Georgiadis, D.; Stratikos, E.; Stern, L.J. Conformational dynamics linked to domain closure and substrate binding explain the ERAP1 allosteric regulation mechanism. *Nat Commun* **2021**, *12*, 5302, doi:10.1038/s41467-021-25564-w.
47. Papakyriakou, A.; Stratikos, E. *The role of conformational dynamics in antigen trimming by intracellular aminopeptidases*; 2017; Vol. 8;.
48. Blat, Y. Non-competitive inhibition by active site binders. *Chem. Biol. Drug Des.* **2010**, *75*, 535–540, doi:10.1111/J.1747-0285.2010.00972.X.
49. Pesaresi, A. Mixed and non-competitive enzyme inhibition: underlying mechanisms and mechanistic irrelevance of the formal two-site model. *J. Enzyme Inhib. Med.*

Chem. **2023**, *38*, doi:10.1080/14756366.2023.2245168.
50. Giastas, P.; Mpakali, A.; Papakyriakou, A.; Lelis, A.; Kokkala, P.; Neu, M.; Rowland, P.; Liddle, J.; Georgiadis, D.; Stratikos, E. Mechanism for antigenic peptide selection by endoplasmic reticulum aminopeptidase 1. *Proc. Natl. Acad. Sci. U. S. A.* **2019**, *116*, doi:10.1073/pnas.1912070116.
51. Arya, R.; Maben, Z.; Rane, D.; Ali, A.; Stern, L.J. Phenylsulfamoyl Benzoic Acid Inhibitor of ERAP2 with a Novel Mode of Inhibition. *ACS Chem. Biol.* **2022**, *17*, 1756–1768, doi:10.1021/acschembio.2c00093.
52. Liddle, J.; Hutchinson, J.P.; Kitchen, S.; Rowland, P.; Neu, M.; Cecconie, T.; Holmes, D.S.; Jones, E.; Korczynska, J.; Koumantou, D.; et al. Targeting the Regulatory Site of ER Aminopeptidase 1 Leads to the Discovery of a Natural Product Modulator of Antigen Presentation. *J. Med. Chem.* **2020**, *63*, 3348–3358, doi:10.1021/acs.jmedchem.9b02123.
53. Stamogiannos, A.; Maben, Z.; Papakyriakou, A.; Mpakali, A.; Kokkala, P.; Georgiadis, D.; Stern, L.J.L.J.; Stratikos, E. Critical Role of Interdomain Interactions in the Conformational Change and Catalytic Mechanism of Endoplasmic Reticulum Aminopeptidase 1. *Biochemistry* **2017**, *56*, doi:10.1021/acs.biochem.6b01170.
54. Yang, L.; Antonelli, S.; Chodankar, S.; Byrnes, J.; Lazo, E.; Qian, K. Solution scattering at the Life Science X-ray Scattering (LiX) beamline. *J. Synchrotron Radiat.* **2020**, *27*, 804–812, doi:10.1107/S1600577520002362.
55. Yang, L.; Lazo, E.; Byrnes, J.; Chodankar, S.; Antonelli, S.; Rakitin, M. Tools for supporting solution scattering during the COVID-19 pandemic. *J. Synchrotron Radiat.* **2021**, *28*, 1237–1244, doi:10.1107/S160057752100521X.
56. Manalastas-Cantos, K.; Konarev, P. V; Hajizadeh, N.R.; Kikhney, A.G.; Petoukhov, M. V; Molodenskiy, D.S.; Panjkovich, A.; Mertens, H.D.T.; Gruzinov, A.; Borges, C.; et al. ATSAS 3.0: expanded functionality and new tools for small-angle scattering data analysis. *J. Appl. Crystallogr.* **2021**, *54*, 343–355, doi:10.1107/S1600576720013412.

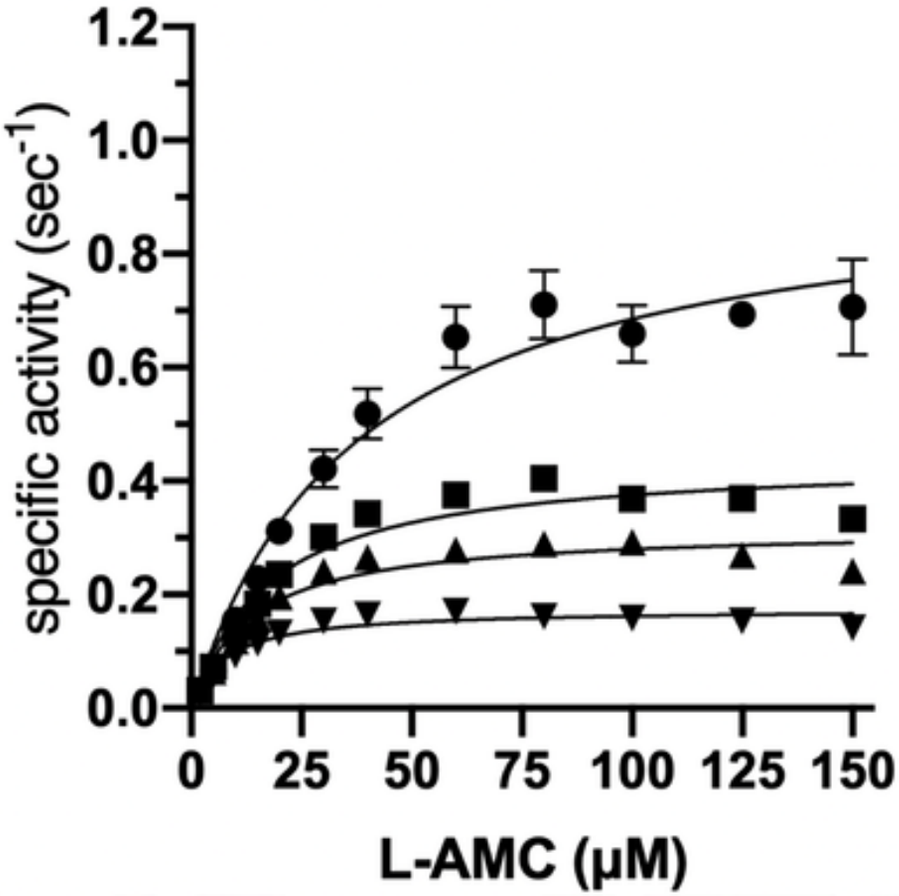
specific activity (sec-1)
1.2
1.0
0.8
0.6
0.4
0.2
0.0
0
25
50
75
100
125
150
L-AMC (μM)

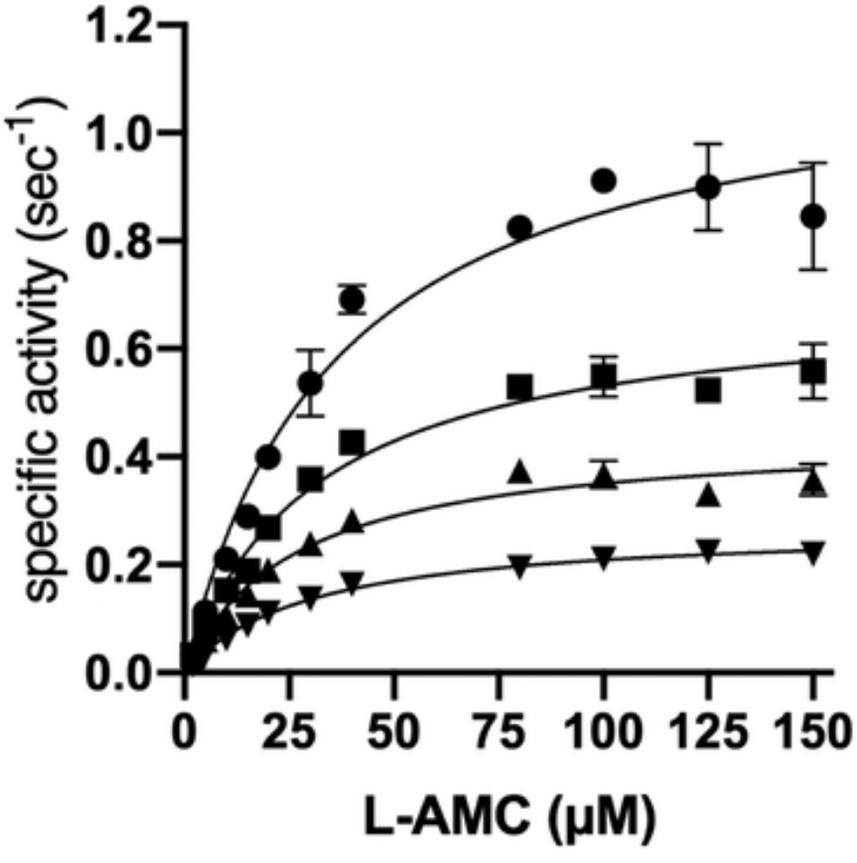
specific activity (sec-1)
1.2
1.0
0.8
0.6
0.4
0.2
0.0
0
25
50
75
100
125
150
L-AMC (μM)

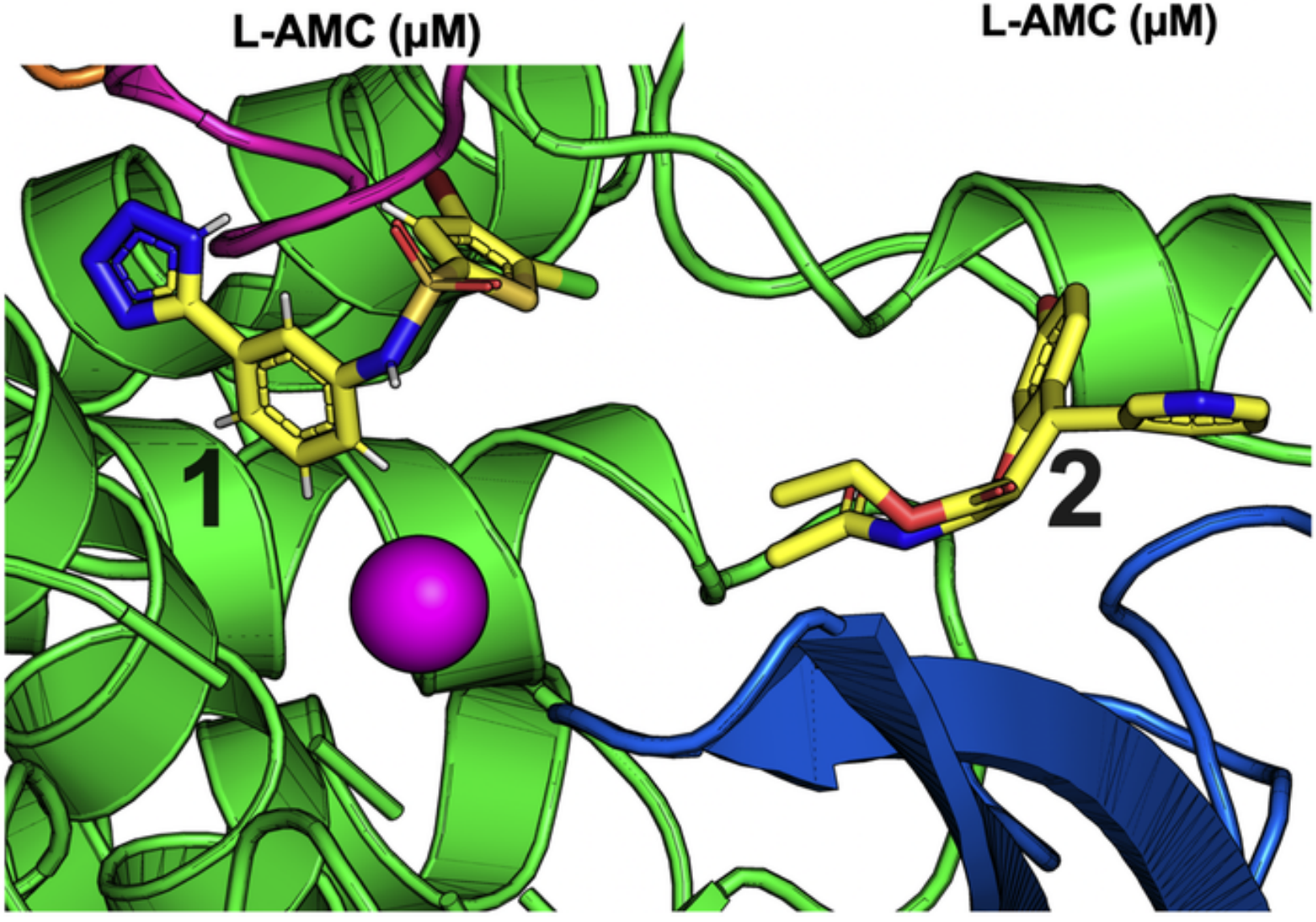
1
2